New Constraints on the Volatile Deposit in Mercury's North Polar Crater, Prokofiev

Michael K. Barker[a], Nancy Chabot[b], Erwan Mazarico[a], Matthew Siegler[c,d], Jose M. Martinez-Camacho[c,d], Colin Hamill[e], Stefano Bertone[f]

[a]NASA Goddard Space Flight Center, 8800 Greenbelt Rd., Greenbelt, MD 20771, USA

[b]Johns Hopkins Applied Physics Laboratory, 11100 Johns Hopkins Rd., Laurel, MD 20723, USA

[c]Planetary Science Institute, 1700 East Fort Lowell, Suite 106, Tucson, AZ 85719, USA

[d]Southern Methodist University, Roy M. Huffington Department of Earth Sciences, 6425 Boaz Lane, Dallas, TX 75205, USA

[e]Purdue University, Department of Earth, Atmospheric, and Planetary Sciences, 550 Stadium Mall Dr., Lafayette, IN 47907, USA

[f]University of Maryland Baltimore County, 1000 Hilltop Cir., Baltimore, MD 21250, USA

Corresponding author: Michael K. Barker (Michael.k.barker@nasa.gov)

Abstract

We present new high-resolution topographic, illumination, and thermal models of Mercury's 112 km-diameter north polar crater, Prokofiev. The new models confirm previous results that water ice is stable at the surface within the permanently shadowed region (PSR) of Prokofiev for geologic timescales. The largest radar-bright region in Prokofiev is confirmed to extend up to several kilometers past the boundary of its PSR making it unique on Mercury for hosting a significant radar-bright area outside a PSR. The near-infrared normal albedo distribution of Prokofiev's PSR suggests the presence of a darkening agent rather than pure surface ice. Linear mixture models predict at least roughly half of the surface area to be covered with this dark material. Using improved altimetry in this crater, we place an upper limit of 26 m on its ice deposit thickness. The 1 km-baseline topographic slope and roughness of the radar-bright deposit are lower than the non-radar-bright floor although the difference is not statistically significant when compared to the non-radar-bright floor's natural topographic variations. These results place new constraints on the nature of Prokofiev's volatile deposit that will inform future missions, such as BepiColombo.

Keywords: Polar illumination; Mercury; Ice; Volatiles; Permanently shadowed regions

1 Introduction

Due to Mercury's low obliquity, its poles host permanently shadowed regions (PSRs) where temperatures can reach below ~110 K and where water ice and other volatiles could be stable for billions of years. Indeed, there is strong evidence from multi-wavelength, multi-instrument observations and thermal models for the presence of such volatiles in Mercury's north polar PSRs. Ground-based radar measurements identified areas as having backscatter characteristics consistent with ~95% pure ice deposits at least several meters thick on or near the surface (Butler et al. 1993; Harmon 2007; Harmon et al. 2011), which spatially correlate with some, but not all, PSRs identified using MESSENGER data (Deutsch et al. 2016). The Mercury Laser Altimeter (MLA) onboard the MESSENGER spacecraft found that some of the radar-bright deposits appeared bright at 1064 nm while others appeared dark (Neumann et al. 2013). Thermal models based on an MLA-derived polar digital elevation model (DEM) predicted that ice would be stable for geologic timescales on the surfaces of the MLA-bright regions whereas ice would have to lie ~ 10 cm beneath the surface to be long-lived in the MLA-dark regions (Paige et al. 2013). The MESSENGER Gamma Ray and Neutron Spectrometer measured epithermal and fast neutron suppression at the poles consistent with an average two-layer stratigraphy in all the radar-bright regions in which the upper layer was ~10 – 30 cm thick with 0 – 25 wt% water equivalent hydrogen (WEH) and the lower layer was more than tens of cm thick with 12 – 100 wt% WEH (Lawrence et al. 2013). The MESSENGER Mercury Dual Imaging System (MDIS) acquired broadband visible images of PSRs when they were illuminated by scattered light from surrounding terrain, revealing a similar pattern as seen by MLA: dark regions inside radar-bright areas too warm to host stable surface ice and an anomalously bright region in the 112 km-diameter crater, Prokofiev, co-located with a radar-bright and MLA-bright area cold enough to host stable surface ice (Chabot et al. 2014). Most recently, Rivera-Valentín et al. (2022) analyzed new radar data and identified variations in radar scattering behavior between and within the polar deposits indicative of variations in ice purity independent of their brightness at optical wavelengths. They found that although most radar-bright regions were consistent with highly pure ice, some areas, such as Prokofiev's optically bright region, had radar scattering properties consistent with a higher fraction of impurities relative to other nearby areas. Altogether, the observations to date have painted a broadly consistent picture in which the north polar radar-bright regions are predominantly highly pure water ice at least several meters thick. These ice deposits appear optically bright where they are predicted to be exposed at the surface and optically dark where they are modeled to be overlain with an insulating layer of complex organic volatiles typically tens of cm thick that formed as a thermal lag after the surface and near-surface ice sublimated (Paige et al. 2013).

One open question concerned the observation that the boundary of Prokofiev's optically-bright region was offset by several kilometers inward from the edges of both its radar-bright region and its PSR

estimated from MDIS imaging (Chabot et al. 2014). Such an offset, if true, could have implications for the ice properties and its delivery and destruction mechanisms. For example, lateral mixing by impact gardening was hypothesized to have covered the outer edge of the surface ice leading to the boundary offset (Chabot et al. 2014). However, the boundary of the optically-bright region closely matched the PSR computed with an alternative method based on the polar MLA DEM (Neumann et al. 2013; Deutsch et al. 2016). If there really is an offset between the PSR and radar-bright boundaries, then this area would be unique on Mercury since all other large radar-bright regions are closely associated with PSRs (Deutsch et al. 2016), including Mercury's south polar region (Chabot et al. 2018a). Such an offset could have implications for the ice deposit characteristics, like depth, age, and evolution. It was unclear whether the MDIS images were sufficiently sensitive to detect dimly sunlit areas along the margins of the radar-bright region when building the MDIS-based PSR map (Chabot et al. 2014). This could lead to an overestimate of the PSR size. Additionally, inaccuracies in the low-resolution MLA DEM (500 m pix^{-1}), particularly on the crater wall, could have caused the MLA-based PSR to be too small (Deutsch et al. 2016). Improved topographic and illumination models were, therefore, needed to settle the question of the true extent of Prokofiev's PSR. In the present work, we address these issues by developing new higher-resolution and more accurate topographic, illumination, and thermal models of Prokofiev.

In addition, previous work has noted that the MLA-bright polar regions have a reflectance value of ~0.4, roughly ~2 times brighter than average Mercury regolith (Neumann et al. 2013; Deutsch et al. 2017; Rubanenko et al. 2018). This fact suggests the presence of a darker material to reduce the observed MLA reflectance below the expected value of ~1.0 for pure ice. The composition and abundance of this dark material are unknown but can help constrain the origin and evolution of the ice and dark material. Therefore, we also study the MLA reflectance data in Prokofiev to quantitatively estimate the ice and dark material's abundances.

Other recent work on the Moon and Mercury's PSRs has found evidence that ice or sub-surface ice may affect surface geomorphologic characteristics. This evidence includes smaller depth-to-diameter ratios of craters hosting PSRs and lower surface roughness inside PSRs compared to outside PSRs (e.g., Rubanenko et al. 2019; Moon et al. 2021; Deutsch et al. 2021a; Deutsch et al. 2021b). Studies have also estimated the average thickness of Mercury's polar ice deposits to be 50 ± 35 m (Eke et al. 2017) and 41^{+30}_{-14} m (Deutsch et al. 2018). Susorney et al. (2019) placed a tighter upper limit of 15 m on the average thickness in 4 north polar craters including Prokofiev where they estimated a thickness of 36 ± 60 m. Here we use a similar approach and a more comprehensive set of improved MLA tracks for this crater to examine whether the ice deposit has any topographic expression in terms of surface height, slope, and roughness.

This paper is organized as follows: In Section 2, we describe the new topographic, thermal and illumination models. Then, in Section 3, we apply linear mixture models to the MLA reflectance data in Prokofiev to constrain the abundance of surface ice and dark material. In Section 4, we examine the

topography of the volatile deposit. In Section 5, we discuss the results and implications for Prokofiev's volatile deposit and compare it to the Moon. Finally, we summarize the results in Section 6.

2 New Topographic, Illumination and Thermal Models

Previously, Hamill et al. 2020 (hereafter H20) derived new topographic, illumination, and thermal models for 8 northern craters hosting dark surface deposits. Here, we follow the same procedures used by H20 to derive new models for Prokofiev. We used MLA altimetry and MDIS images together with the Ames Stereo Pipeline (ASP) shape-from-shading (SfS) tool (Alexandrov & Beyer 2018). The ASP SfS tool uses the technique of photoclinometry to derive a topographic model based on the pixel shading variations observed in images. The tool requires an initial *a priori* model, for which we used a locally optimized MLA-only DEM obtained by bundle adjustment of the MLA tracks in a manner similar to that used with Lunar Orbiter Laser Altimeter data for the lunar crater, Shackleton (Zuber et al. 2012). For the image data, we used a set of 34 MDIS images of Prokofiev with pixel scales of ~70 to 170 m pix^{-1} sampling a wide range of Sun azimuth.

The final hybrid MLA+SfS DEM (Figure 1a), with a pixel scale of 125 m pix^{-1}, is more complete than either an MDIS-only or MLA-only DEM alone. The MLA-only DEM fills in areas shadowed in all images (including PSRs) which correspond to most of the southern half of the crater floor, while the images provide denser coverage of illuminated terrain including the crater rim, which is important for determining the true extent of PSRs. The topography of Prokofiev's floor is relatively flat on large baselines, but numerous small craters give it a mottled appearance. Some fraction of these craters are likely secondaries from Kandinsky indicating that the surface ice in Prokofiev must post-date that crater (Chabot et al. 2014).

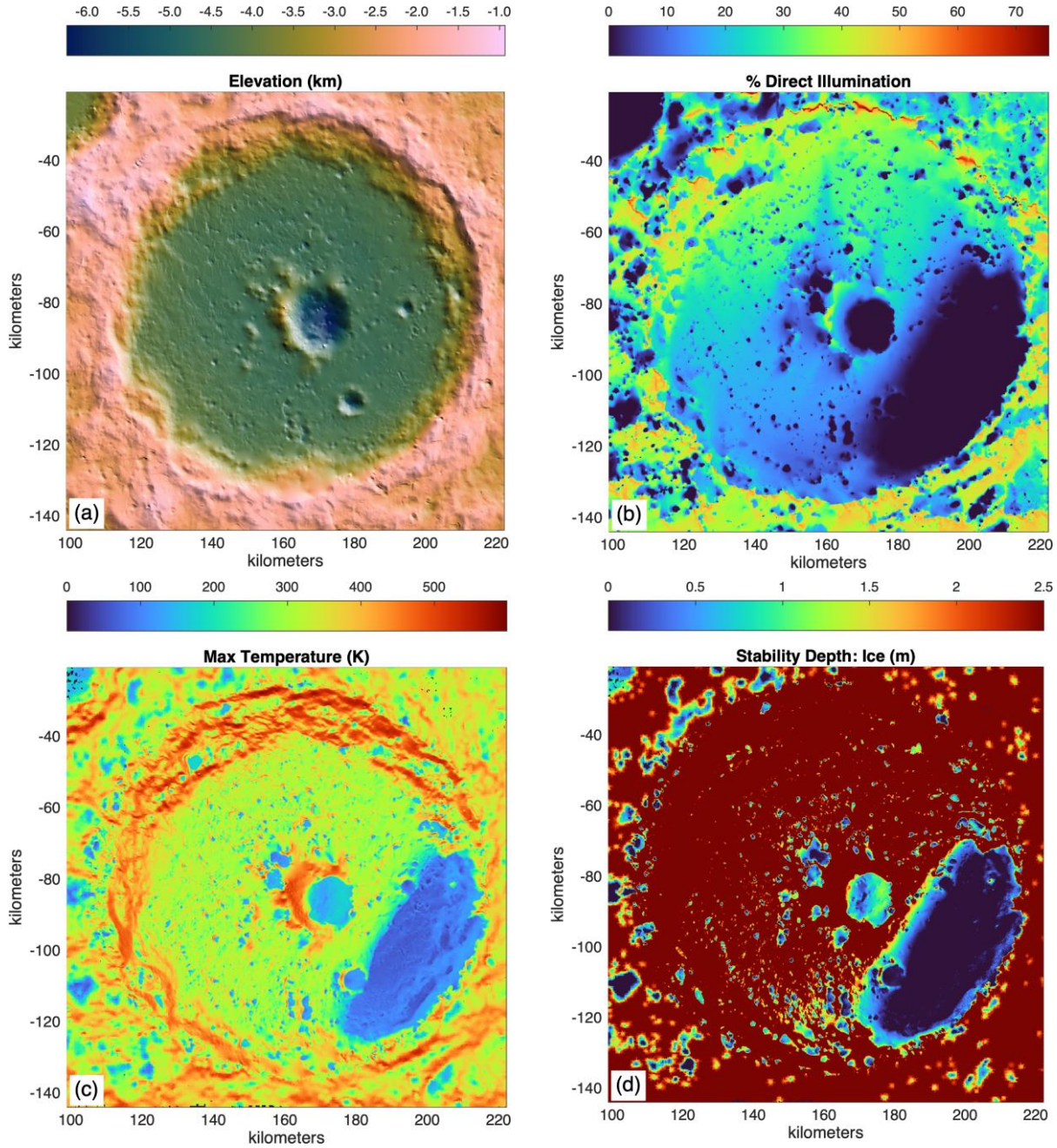

Figure 1 – High-resolution polar stereographic models of Prokofiev at 125 m pix^{-1} with the origin at the north pole and 0° longitude to the bottom. (a) Colorized hillshade of MLA+SfS DEM. (b) Average illumination over one Mercury solar day. Dark blue regions are PSRs. (c) Maximum surface temperature throughout a Mercury solar day. (d) Depth below the surface needed for the long-term stability of ice. Dark blue regions are areas where ice is thermally stable at the surface. Dark red areas are where no ice is stable within the upper 2.5 m, and generally, therefore, where ice is unstable at any depth.

This new topographic model allows a more detailed look at the illumination and thermal conditions inside Prokofiev than was previously possible with the polar MLA DEM. To that end, we ran illumination and thermal models using the same approach as in H20. The illumination model computed the direct incident solar flux and fraction of the Sun (treated as a 2-dimensional limb-darkened source) visible at hourly timesteps for a whole Mercury day (~176 Earth days). The thermal model and its parameters (0.04 albedo, 0.9 emissivity, and a two-layer temperature dependent thermal inertia) follows Paige et al. (2010, 2013) and accounts for reflected visible and reradiated infrared radiation to produce temperature profiles (here, to 2.5 m depth, several times the thermal skin depth). Solar declination and obliquity were taken from the JPL Horizons[1] ephemeris. Ice stability depth is calculated assuming lunar regolith diffusion (Schorghofer and Taylor, 2007) to find the depth at which ice would be lost at a rate of 1 m Gyr^{-1}. The properties of Mercury's regolith and the potential presence of complex organics as observed in other PSRs might make the conditions within Prokofiev different than the lunar regolith model. However, given our limited knowledge about Mercury's regolith and composition, application of the lunar regolith model to Mercury is appropriate. Dark material overlying subsurface ice may be more or less porous than regolith, but due to the exponential dependence of volatile loss on temperature, this does not substantially affect the stability boundaries, which appear to align well with the regolith assumption. Finally, all thermal and illumination model calculations were done in 3-dimensional Cartesian coordinates and treated the Sun as a 2-dimensional limb-darkened source sub-divided into 128 sub-sources with full 3-dimensional ray-tracing from each. Thus, the models account for the planet's curvature and penumbral effects.

The PSRs within Prokofiev appear as dark blue regions in the map of average illumination (Figure 1b) and are dominated by a large area along the southern portion of the crater and the central peak-ring crater, with many smaller PSRs distributed throughout the floor inside the aforementioned small craters. The large southern PSR also stands out in the thermal model with maximum temperature $T_{max} < 110$ K (Figure 1c), and surface-stable ice (i.e., stability depth of 0 m in Figure 1d). The central crater and most of the resolved smaller floor craters are too warm for stable surface ice. Note, however, that stable surface ice may exist in smaller cold traps unresolved by the DEM (Rubanenko et al. 2018).

[1] https://ssd.jpl.nasa.gov/horizons/

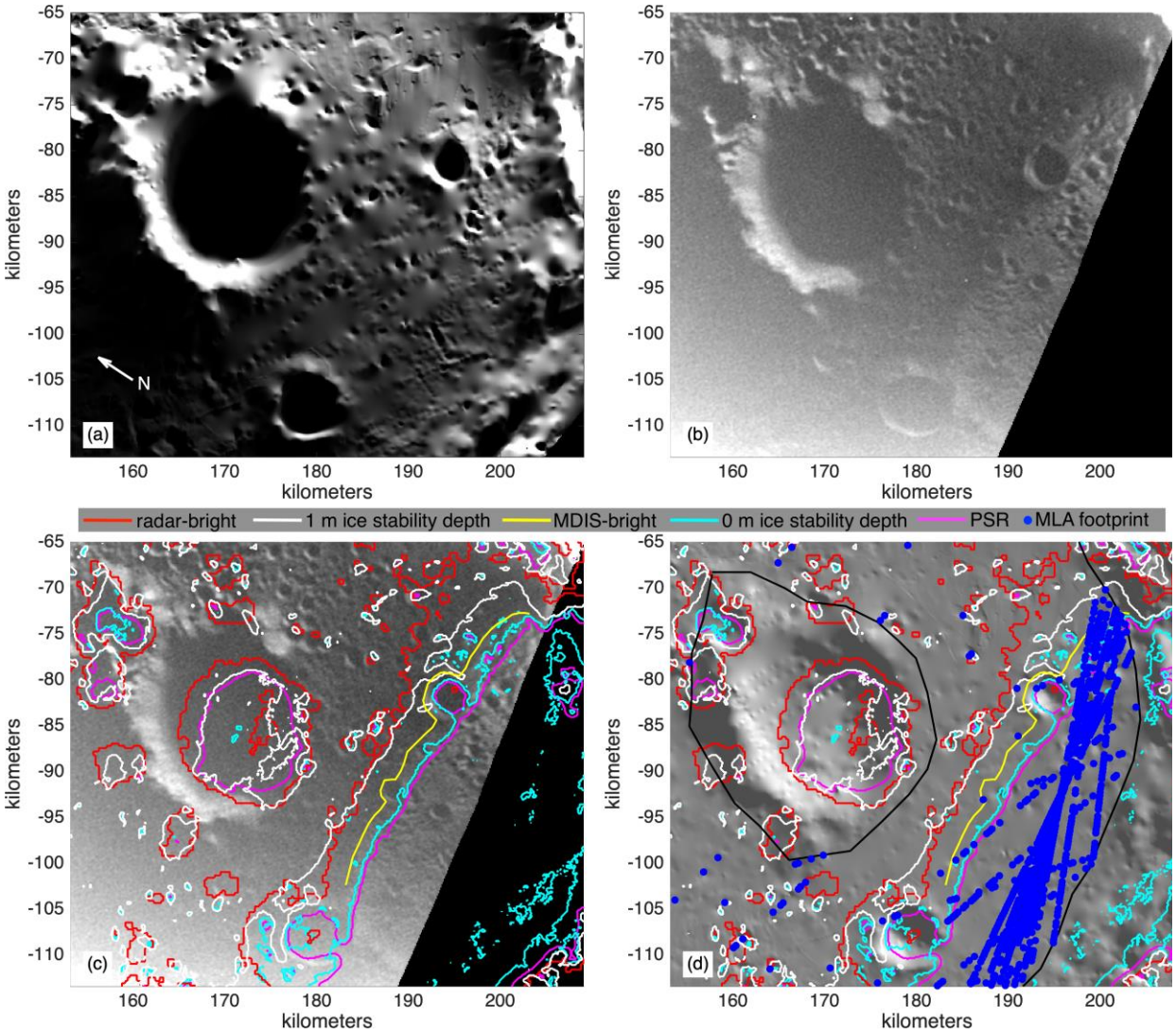

Figure 2 – Comparison between models (125 m pix^{-1}) and MDIS broadband image EW1020581108B (188 m pix^{-1}) in stereographic projection with the origin at the north pole and 0° longitude to the bottom. (a) Simulated image using the MLA+SfS DEM, (b) MDIS image, (c) MDIS image with contours: PSR (magenta), ice stability depth of 0 m (cyan), MDIS-bright boundary (yellow), ice stability depth of 1 m (white), and radar bright region (red), (d) hillshade of the MLA+SfS DEM with the same contours and black lines defining the inner and outer edge of the floor region used to select MLA reflectance footprints (blue points) for the mixture modeling in Section 3.

Figure 2a shows a simulated image that includes scattered light within the crater at the acquisition time of the broadband MDIS image in Figure 2b when the sub-solar latitude and longitude were 0.008° north and 335.593° east, respectively. A Lambertian surface was assumed although we also tried a Hapke reflectance law tailored to Mercury (Domingue et al. 2016) which resulted in an insignificant

change. The simulation does not include instrumental stray light responsible for the large-scale gradient from bottom to top of the MDIS image as oriented in Figure 2b. A quantitative comparison between the acquired MDIS image and the simulated image is hampered by the lack of an absolute radiometric calibration for the WAC broadband filter (Denevi et al 2018). Nevertheless, the simulated image generally reproduces well the reflectance variations associated with topography particularly around the rim of the central peak. However, it does not exhibit the MDIS-bright region on the floor associated with the PSR. This confirms earlier lower resolution scattered light simulations based on the polar MLA DEM that could not reproduce this bright region (Chabot et al. 2014), and strongly supports that it is a real feature on the surface rather than a result of the natural topography and the diffuse lighting conditions.

The higher resolution and fidelity of the new models allow a more detailed examination of the PSR and MDIS-bright boundaries than previously possible. Figure 2c overlays on the MDIS image contours representing PSRs (magenta), 0 m ice stability depth (cyan), the MDIS-bright boundary (yellow), 1 m ice stability depth (white), and radar brightness of 4σ above the background (red) computed from a weighted sum of 13 Arecibo observations in the period 1999 – 2005 (Figure 3b of Harmon et al., 2011).

Several key points are evident in Figure 2. First, the radar-bright boundary extends up to several km outside the PSR (and MDIS-bright region). This strongly favors the interpretation that this boundary offset is real and not an artifact of inaccuracies in the MLA-only or MLA+SfS DEMs or in the ability to register the radar and MESSENGER datasets and makes this region unique on Mercury for hosting a substantial radar-bright area outside a PSR. This transition zone from the edge of the PSR to the edge of the radar-bright region is unlikely to be a radar beam-smearing effect since the area is larger than the radar resolution of 1.5 km (Harmon et al. 2011). If radar clutter due to the high incidence angle was artificially boosting the signal in this region, then that would apply to radar-bright regions everywhere on Mercury, and every radar-bright region would extend well beyond the PSR. But in fact, we do not see that and only see it for this region in Prokofiev (Deutsch et al. 2016). Volume scattering off wavelength-scale rocks and bedrock fractures below the surface may be contributing to the apparent radar brightness. However, sub-surface ice appears to be a simpler explanation for the radar-bright unit outside the PSR because it is predicted by the thermal models, which are generally supported by the observational evidence for ice below and on the surface in Mercury's PSRs as summarized in Section 1. The ice stability depth in this transition zone reaches up to ~1 – 2 m, suggesting that any sub-surface ice would have to be thick enough to appear as radar-bright through the radar-attenuating dry upper layer. The dry upper layer here may be less attenuating compared to the polar average or there may be ice closer to, or even exposed on, the surface inside small-scale cold traps unresolved by the models (Rubanenko et al. 2018). However, any surface ice in this zone outside the MDIS-bright boundary must also be obscured from view or too faint to be visible in the MDIS image (the coldest surfaces most likely to host ice also receive less scattered light and therefore contribute fewer photons to passive imagers). Notably, the MLA reflectance inside this transition zone is anomalously bright and similar to that in the PSR region (see

Section 3), but most of the MLA footprints here lie in a small cluster between the PSR and MDIS-bright boundaries at map coordinates (200 km, -75 km) in Figure 2d. Therefore, we cannot say for certain if there is stable surface ice in small-scale cold traps beyond the MDIS-bright region.

Second, the MDIS-bright boundary in Figure 2 extends ~1.0 km farther than the stable surface ice boundary. This offset is about 3 times larger than the estimated registration accuracy based on manual feature matching between the MDIS and simulated images. If the MDIS-bright region hosts stable surface ice, then this discrepancy could be due to several factors, such as the ice not yet having reached equilibrium, topographic effects below the resolution of the DEM, or choices of parameters within the thermal model. This could imply some form of vertical migration of ice from the subsurface, such as impact gardening or thermal diffusion, that exceeds the rate of surface loss in these areas. Also, as previously mentioned, sub-resolution topographic roughness could make stable surface ice more likely to exist beyond where the current 125 m pix^{-1} thermal model predicts. This explanation may require further study, however, since the small-scale slopes would need to be oriented both to avoid all but the briefest periods of direct sunlight during the Mercury day and to be observable from the position of MESSENGER at the time of the MDIS image in Figure 2b. The small-scale slopes would also have to receive enough scattered radiation to be detectable by MDIS during the acquisition of the image in Figure 2b but not so much as to lead to maximum temperatures > 110 K which would rapidly sublimate the ice. Additionally, the thermal model has several parameters that were tuned to lunar regolith which could be different for Mercury's regolith. Variations in certain parameters (e.g., thermal conductivity), which could be caused by the ice itself, could cause the model's stable surface ice boundary to be larger or smaller. Also, the model assumes that the maximum temperature ever experienced controls the ice loss rate. Ice might only experience that maximum temperature for a short period making the time-integrated loss rate more appropriate (Schorghofer & Williams 2020).

Finally, out of all the contoured regions, the PSR has the smallest area and surface ice is modeled to be stable slightly beyond the PSR. This is not altogether unexpected given the low conductivity assumed in the thermal model and it demonstrates that surface ice can withstand small amounts of sunlight. Indeed, the ~500 m wide gap between the PSR and surface ice stability contours experiences < 1% solar illumination (<100 W m^{-2}) during a single period with duration < 1 Earth day during every Mercury solar day (176 Earth days). H20 observed similar behavior in dark deposit craters where the dark surface volatile deposits can extend past the PSRs by as much as ~1 km, farther than ice here due to the higher inferred stability of the dark deposit compounds.

3 Mixture Modeling

To constrain the ice abundance, we use the MLA reflectance, or normal albedo, since it is observed at a phase angle of zero degrees and is thus free from the confounding effects of illumination

geometry and scattered light (Neumann et al. 2013). Nevertheless, the MLA reflectance[2] was a noisy measurement with systematic instrumental errors necessitating manual selection of a reliable subset of data. By examining the dependence of the MLA reflectance on various instrument-related parameters, we found that including only pulse widths of 15 – 90 ns, ranges of 100 – 800 km, and emission angles < 20° removed noisy measurements and outliers and yielded a reasonably consistent set of measurements (Figure 3). The reason for the pulse width behavior in Figure 3 (left panel) is not entirely clear, but it may be related to the fact that the MLA reflectance is based on the difference in pulse width measured at a pair of thresholds. Noise, sub-optimal system response, non-ideal operating conditions, and degradation of the transmitted pulse may cause errors in the pulse width estimation, thus impacting the derived reflectance (Neumann et al. 2013; Sun & Neumann 2015). The secondary trend visible in light blue below the main trend in Figure 3 (left panel) is due to the data with range < 100 km (seen in the middle panel). The global mode of the MLA reflectance (~0.17) is within 20% of the 996 nm normal albedo predicted by MDIS-based photometric models (Domingue et al. 2016), so we take 20% as the absolute uncertainty. Also, the spread in MLA reflectance about the mean is about 25% globally in individual bins of size 0.1x0.1 degrees (~4x4 km at the equator). Given that some of that variance is geological, it is roughly consistent with a 20% instrumental error.

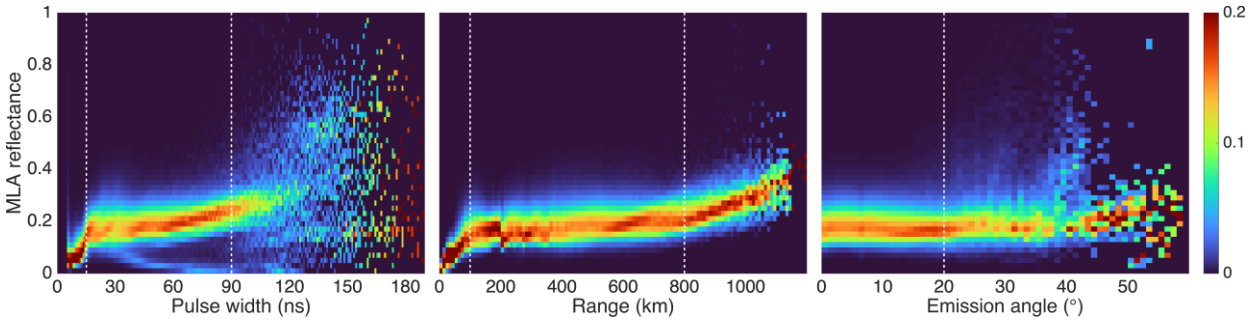

Figure 3 – 2-dimensional histograms of MLA reflectance as a function of pulse width (left), range (middle), and emission angle (right) for latitudes 55 – 83°. The color scale gives the fraction of the number of points in each column of each histogram. The y-axis bin size is 0.02 and the x-axis bin size is 1 ns, 10 km, and 1°. The dashed white lines show the adopted thresholds used for extracting good data: pulse width = 15 – 90 ns, range = 100 – 800 km, and emission angle < 20°. The middle and right panels have had the pulse width and pulse width + range cuts applied, respectively.

Figure 4 compares the resulting MLA reflectance distribution for several different areas relevant to our analysis: 1) Prokofiev's floor outside both the MDIS-bright region and PSRs ("non-MDIS-bright,

[2] RADR v4 data available at the NASA Planetary Geodesy Data Archive (https://pgda.gsfc.nasa.gov) at Goddard Space Flight Center

non-PSR", orange line, 83 points total), 2) Prokofiev's floor inside the MDIS-bright region but outside PSRs ("MDIS-bright, non-PSR", black line, 95 points), 3) Prokofiev's floor PSRs ("PSR", cyan line, 833 points), 4) a nearby control sample outside Prokofiev ("nearby Prokofiev", red line, 4126 points), and 5) PSRs of the 8 H20 dark deposit craters ("dark deposit", blue line, 1662 points). The peak in the reflectance distribution outside Prokofiev's floor PSRs and MDIS-bright region (orange line) is consistent with the nearby control sample (red line) and global value suggesting that the majority of Prokofiev's sunlit floor is representative of average Mercury regolith whereas the peak of ~0.4 for the distribution inside floor PSRs (cyan line) is ~2x brighter as noted in previous work (Neumann et al. 2013, Chabot et al. 2014). Additionally, the MLA reflectance distribution in the narrow MDIS-bright region outside PSRs (black line) is consistent with the one inside PSRs although, as noted in Section 2, the spatial sampling of MLA reflectance in this region is limited (Figure 2d).

The fact that the PSR reflectance is much smaller than the expected value of ~1.0 for pure ice suggests the presence of a darkening agent mixed with the ice. The abundance and form of the mixture (e.g., areal or intimate) is unknown. Here, we assume a checkerboard areal mixture model in which each photon interacts only with ice or the darker material and, hence, the observed reflectance is the linear combination of the reflectance values of these end-members weighted by their fractional areal coverage (Hapke 2012).

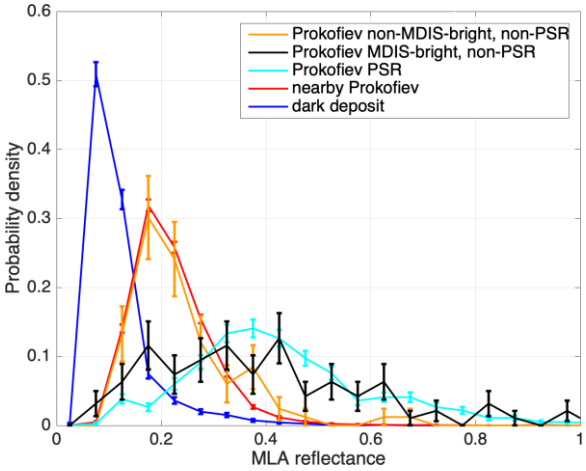

Figure 4 – Distribution of MLA reflectance for 1) Prokofiev's floor outside both the MDIS-bright region and PSRs ("non-MDIS-bright, non-PSR", orange), 2) Prokofiev's floor inside the MDIS-bright region but outside PSRs ("MDIS-bright, non-PSR", black), 3) Prokofiev's floor PSRs ("PSR", cyan), 4) a nearby control sample outside Prokofiev ("nearby Prokofiev", red), and 5) the 8 H20 dark deposit PSRs ("dark deposit", blue). Each histogram has a bin size of 0.05 and is normalized by its total number of points. The error bars are Poisson errors.

Initially, we assume all of the MLA footprints (each ~30 – 40 m in diameter) contain this mixture and that the dark and icy end-member reflectances are simple delta-functions. This allows a first-pass estimate of the sub-footprint ice areal fraction, f_i. We set the ice reflectance, r_i, to 0.8, the optimal value

Fisher et al. (2017) derived by fitting the Lunar Orbiter Laser Altimeter (LOLA) reflectance data of the Moon's south polar PSRs. Two different choices for the dark end-member reflectance are likely to encompass the range of possible values: 1) Prokofiev's non-MLA-bright and non-PSR floor reflectance (~0.17) and 2) the dark deposit PSR reflectance of the H20 craters (~0.08). The darker the non-ice end-member is, the more ice that is required to match the observed PSR reflectance. Given Prokofiev's typical PSR reflectance of ~0.4, the resulting sub-footprint ice areal fraction, f_i, is 0.36 (case 1) and 0.44 (case 2). Increasing (decreasing) r_i by 0.2 decreases (increases) f_i by ~0.1 (~0.2).

Next, we take a more detailed approach by relaxing the assumptions that all MLA footprints contain the mixture and that the end-member reflectances are delta-functions. We fit the PSR reflectance distribution (cyan line in Figure 4) as a linear mixture of 1) "dry" regolith with reflectance distribution given by that outside the MDIS-bright region and PSR (orange line in Figure 5) and 2) pure ice with a Gaussian reflectance distribution with mean r_i and standard deviation σ_i to which a 20% measurement error is added. To keep the ice reflectance distribution symmetric and positive, we restrict it to the range 0.0 to $2r_i$. A fraction F_i of MLA footprints contains the mixture each with a sub-footprint areal ice fraction f_i, while the remaining fraction (1-F_i) of footprints have only the darker non-ice material. Figure 5 shows the effects of varying these model parameters. A wide range of f_i and r_i produce acceptable fits since they are highly correlated. Thus, we fix r_i at 0.8 as in the first-pass estimates above. The model is fitted to the data using a χ^2 cost function minimized over a grid in the parameters with step sizes of 0.01/0.02/0.025 for $F_i/f_i/\sigma_i$.

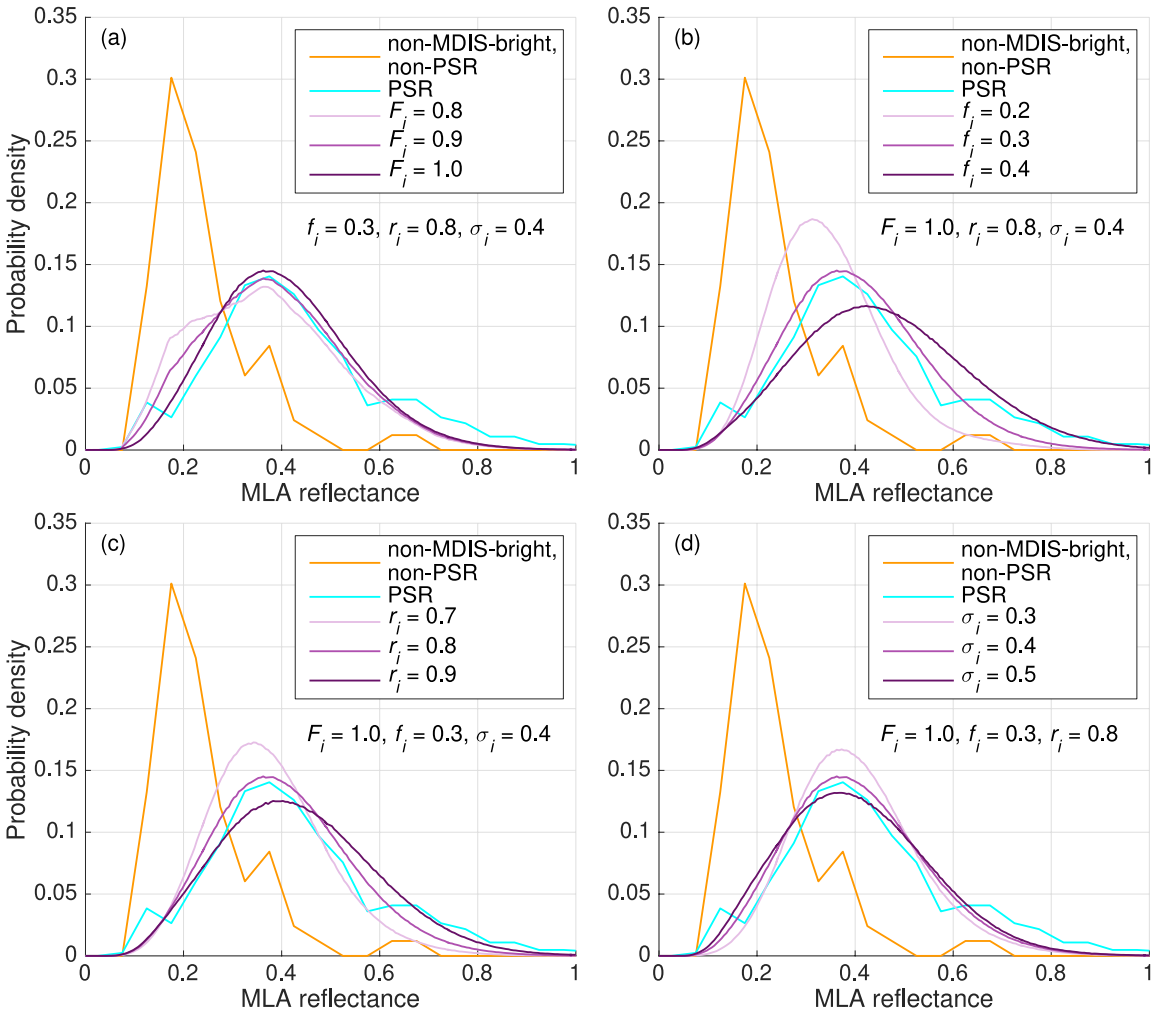

Figure 5 – Effect of varying the mixture model parameters, a) ice-bearing footprint fraction F_i, b) sub-footprint ice fraction f_i, c) mean ice reflectance r_i, and d) ice reflectance spread σ_i. These models use the non-MDIS-bright, non-PSR distribution (orange line) as the dark, non-icy end-member for fitting the PSR distribution (cyan line).

The resulting best-fit model (Figure 6) has F_i = 1.00, f_i = 0.33, and σ_i = 0.40. Reasonable fits can be obtained with F_i in the range ~ 0.83 – 1.00 (1σ), f_i ~ 0.24 – 0.42, and $\sigma_i \gtrsim 0.15$. A high ice-bearing fraction F_i agrees with the broadband MDIS image (Figure 2b) which shows a relatively uniform and continuous ice distribution in the MDIS-bright region at the pixel scale of the image (188 m pix^{-1}).

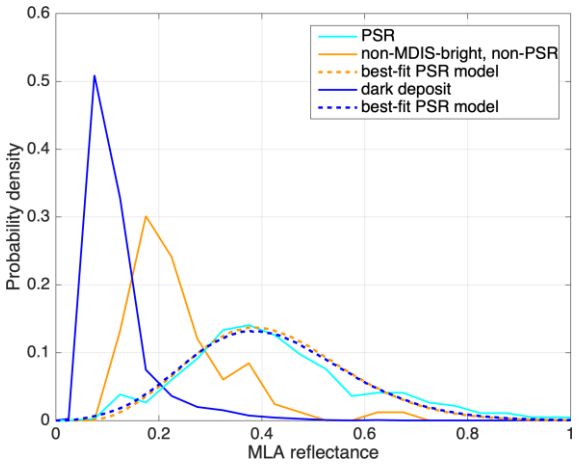

Figure 6 – Best-fit linear mixture models (dashed lines) using (1) the non-MDIS-bright, non-PSR distribution (orange) and (2) dark deposit (blue) as the non-icy end-member to fit the observed PSR distribution (cyan). In both best-fit models, all MLA footprints are ice-bearing (F_i = 1.00) while the sub-footprint ice fraction is (1) f_i = 0.33 and (2) f_i = 0.44.

Rather than average non-PSR regolith, the dark material may consist of the same material that forms the polar dark deposits, hypothesized to be complex organics. To investigate this scenario, we adopt the average PSR reflectance distribution of the 8 H20 craters as the dark end-member. This distribution (Figure 6) has a peak at ~ 0.08 that is narrower than the dry distribution of the previous model. The resulting best-fit looks nearly identical to the previous model and the preferred ice-bearing footprint fraction is F_i = 0.97 – 1.0 with sub-footprint ice fraction f_i = 0.37 – 0.53 and ice reflectance spread σ_i = 0.19 – 0.40.

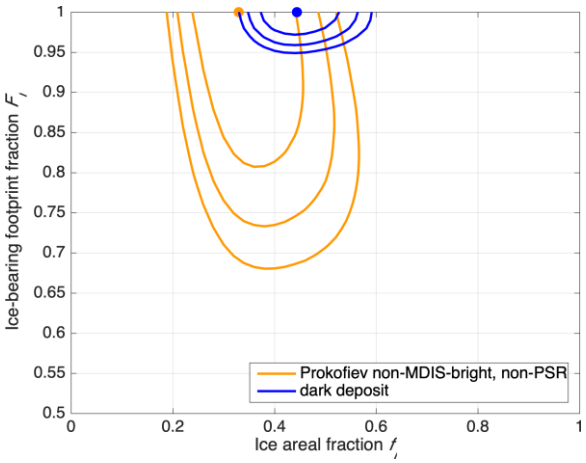

Figure 7 – Best-fit values (solid dots) for the ice-bearing footprint fraction, F_i, and sub-footprint ice areal fraction, f_i, with their respective 1, 2, and 3σ uncertainty contours (innermost to outermost). Two models are shown assuming that the dark end-member's reflectance distribution is the same as that of 1) Prokofiev's floor outside the MDIS-bright region and PSRs ("Prokofiev non-MDIS-bright, non-PSR"; orange lines), or 2) the 8 H20 dark deposits hypothesized to be sublimation lags of complex organics ("dark deposit"; blue lines). In both models, $f_i < 1$ at high confidence meaning pure ice is strongly disfavored.

The results of fitting with the full reflectance distributions are consistent with the first-pass estimates based on delta-functions, but allow a fuller treatment of natural variations in the reflectances and patchiness of the end-members. Taken together, these models suggest that the majority, and likely all, of the MLA footprints in the PSR contain some ice with a sub-footprint areal coverage of at least ~25% and possibly as high as ~50% (Figure 7). The models are inconsistent with $f_i = 1.0$ meaning that pure ice is strongly disfavored. In addition, although we assume nothing about the sizes of the patches in this checkerboard mixing model, we note that $F_i \approx 1.0$ implies that the patches are smaller than the typical MLA footprint size of ~30 – 40 m, which may also explain why the optically bright deposit looks fairly uniform in the MDIS image.

If we relax the assumption that the mean ice reflectance $r_i = 0.8$, then values of f_i between ~0.02 and 1.0 can produce acceptable fits, but they require r_i to be as high as 7.0 and as low as 0.4, respectively. Are such values of ice reflectance reasonable? The single-scattering albedo of pure ice in the near-infrared is likely to be very close to unity (Warren & Brandt 2008). However, the normal albedo can depend on a variety of factors besides the single-scattering albedo, such as the ice grain size, the ice's macroscopic surface roughness and porosity, the opposition effect amplitude, and the ice grain scattering behavior (e.g., the ratio of forward-to-backward scattering in the single particle phase function). Little is known about these properties for space-weathered ice at the relevant environmental conditions. Hence, our assumption of $r_i = 0.8$ seems reasonable at this time. This assumption also facilitates

comparisons between the Moon and Mercury, a point which we discuss in Section 5.

The best-fit models also prefer an ice reflectance spread $\sigma_i \sim 0.2 – 0.4$ implying a non-negligible contribution from values much lower and higher than r_i. An ice reflectance spread may result from natural variations in the ice properties previously mentioned, some of which may be controlled by spatially varying environmental conditions, such as temperature. Alternatively, the sub-footprint ice fraction may vary spatially, mimicking the effect of σ_i with a spread of values for f_i instead.

To investigate the effect of adopting a non-Gaussian reflectance distribution for the pure-ice end-member, we tried a Chi distribution by fixing its reflectance peak at 0.8 and varying its degrees of freedom, k, with the mixture parameters, f_i and F_i. This yielded only a marginally better fit with preferred values of k in the range 2 – 4 (k = 2 for a Rayleigh distribution) and f_i = 0.26 and 0.40, i.e., within 1σ of the best-fit values obtained with a Gaussian (F_i was unchanged). This test shows that the precise shape of the pure-ice reflectance distribution is unlikely to significantly affect the main parameters of interest, f_i and F_i.

One final important caveat is that other types of mixture models, such as intimate mixing and intraparticle mixing (Lucey & Riner 2011), may yield different estimates for the ice abundance than the linear models presented here. Intimate mixing, for example, can hide significantly more ice with a relatively small abundance of dark grains (Hapke 2012; Yoldi et al. 2015). These models contain more free parameters than we can constrain with just one wavelength. Multi-spectral data, such as what will be collected by the Visible and near-Infrared Hyperspectral Imager (VIHI) instrument on the BepiColombo mission, may allow disentangling these other parameters and distinguishing between different types of mixtures (Filacchione et al. 2020), if such measurements of PSR surfaces are possible.

4 Topography of the Volatile Deposit

Next, we look at the elevation trends across Prokofiev's floor to identify signatures of the volatile deposit. We use only the bundle-adjusted MLA altimetry as this provides a consistent set of data both inside and outside the PSRs. First, Mercury's geoid height was subtracted from the altimetry. This amounts to a ~ 30 m trend across the whole DEM in the up-down direction (plan view, as in Figure 1). The resulting mean elevation of the ~4500 MLA footprints outside radar-bright regions within a crater-centric radius of 20 – 38 km is -4107 ± 104 m and the mean elevation of the ~2200 footprints inside radar-bright regions over the same radial range is -4170 ± 67 m. This results in a mean elevation difference of -67 ± 124 m between radar-bright and non-radar-bright regions. Here we consider only crater-centric radii of 20 – 38 km to avoid the central peak ring area and crater walls. We also exclude the two large craters at coordinates (194 km, 179 km) and (-81 km, -108 km) as presented in Figure 1a.

Subtracting a radially-averaged elevation profile reveals a long-wavelength tilt amounting to a ~200 m height decrease across the crater in the direction of roughly 2 o'clock (plan view, Figure 1). This

appears unrelated to the volatile deposit as it is not aligned with the radar-bright region, and it is also present in the sunlit, non-PSR left half (plan view, Figure 1) of the crater. We, therefore, fit a plane to the floor elevation data allowing the crater centroid to vary while minimizing the residuals around the radially averaged profile. Accounting for the long-wavelength tilt and allowing the centroid to move improves the residuals across the entire floor and crater walls.

After subtracting the best-fit plane, the radial profile (Figure 8) shows a small trend of increasing elevation with crater-centric radius which was also evident in the initial profile. The crater centroid moved to (162.976 km, -82.345 km), roughly 2.5 km from its initial location at the central peak (160.464 km, -82.043 km), but closer to the center of the peak ring. The post-fit elevation residuals (Figure 9) are ~2 – 3 times smaller compared to pre-fit and are well-centered on zero with a mean of 0 ± 53 m outside radar-

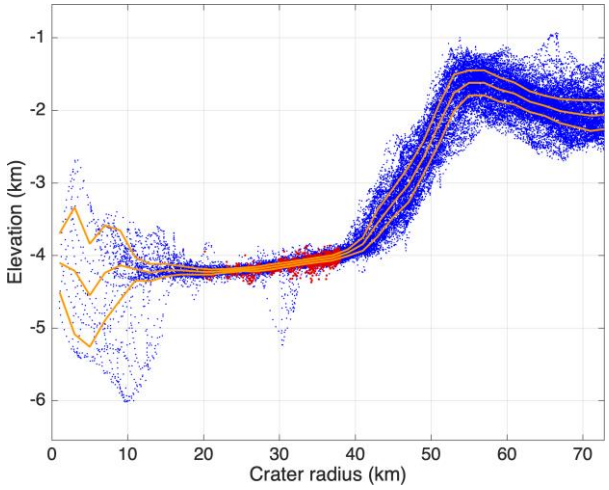

Figure 8 – MLA altimetry (blue points) and best-fit median radial profile and inter-quartile range (orange lines). The red points are the radar-bright MLA footprints.

bright regions and -8 ± 50 m inside radar-bright regions yielding a mean elevation difference of -8 ± 73 m.

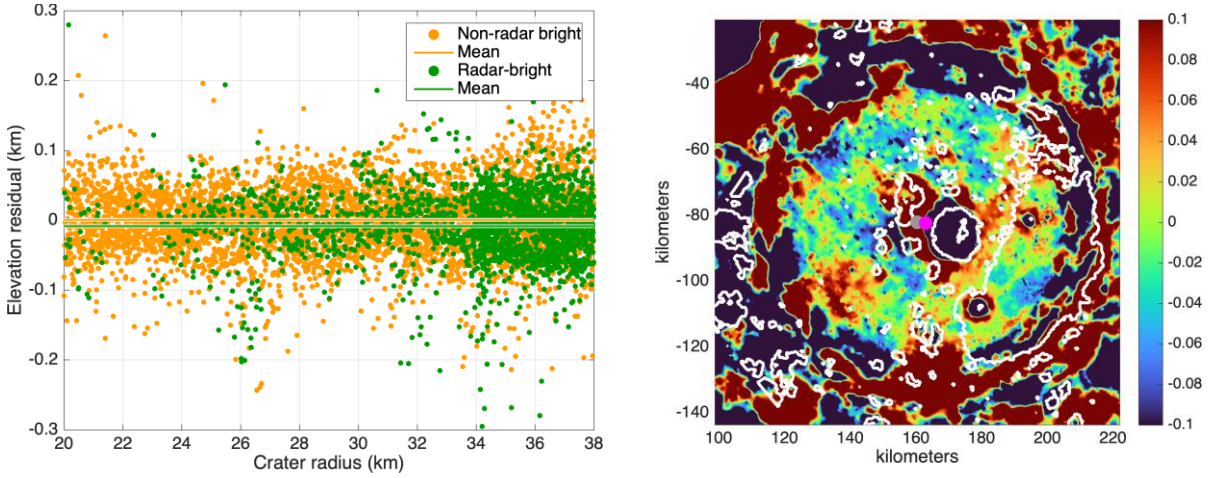

Figure 9 – Left: Elevation residuals of MLA altimetry in radar-bright (green) and non-radar-bright areas (orange) relative to the best-fit radial profile in Figure 8. Right: Elevation residuals (in km) with radar-bright regions overlaid (white lines). The solid gray and magenta circles denote the initial and best-fit crater centroid, respectively.

To place an upper limit on the thickness of the volatile deposit, we wish to test the null hypothesis that the mean elevation residuals are the same inside and outside the radar bright regions. If the null hypothesis is rejected, then that would implicate the ice deposit as the reason for the difference. However, natural topographic variations could also lead to a rejection of the null hypothesis. These variations are spatially correlated over many length scales because the power spectrum of topography on Mercury, and other terrestrial bodies, is not flat as it is for white noise, but rather increases with scale (Shepard et al. 2001; Rosenburg et al. 2011; Susorney et al. 2017). This characteristic is responsible for the similarly-colored contiguous regions (hills and depressions) up to ~10 km in size on the crater floor in Figure 9b. Those patterns could lead us to reject the null hypothesis even without an ice deposit present. If the topographic residuals were uncorrelated (i.e., white noise with a flat power spectrum), then there would be no such spatial patterns. Thus, we need a control sample with similar topographic variations to act as a reference for judging differences between the radar-bright and non-radar-bright regions. Computing bundle-adjusted MLA altimetry for a sample of control craters in the same way as done for Prokofiev is a task beyond the scope of this work. Instead, to account for the extra uncertainty introduced by natural topographic variations, we computed bootstrapped errors by rotating the radar map through 360 degrees in 1000 equally spaced increments and computing the mean elevation residuals for each rotation. The resulting 95th percentile of the difference in mean elevation residual between radar-bright and non-radar-bright regions was 26 m, which we adopt as an upper limit on the thickness of Prokofiev's volatile deposit.

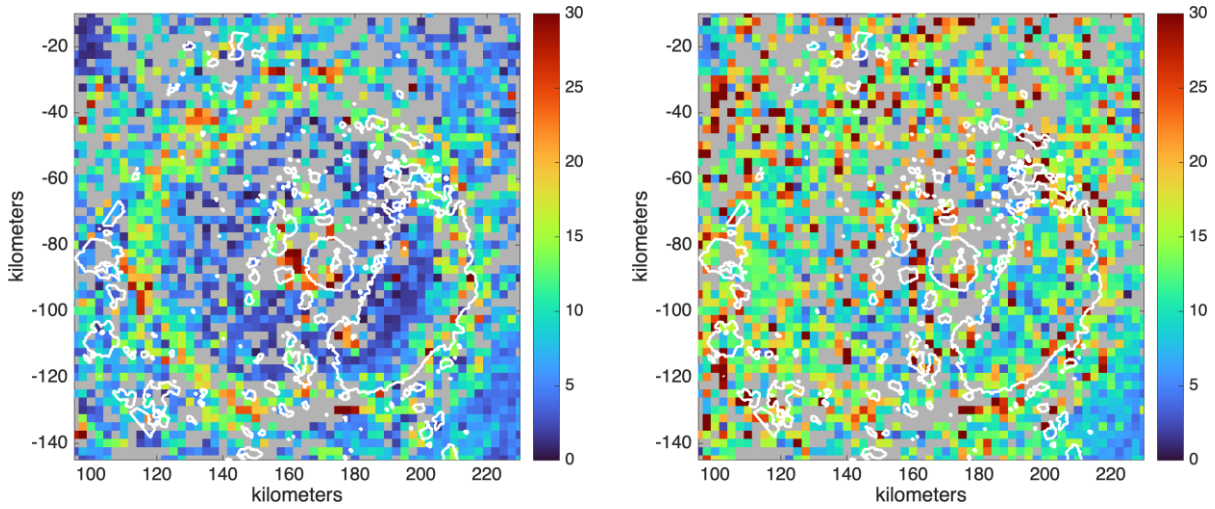

Figure 10 – Left: Slope (in degrees) of plane fits to MLA footprints over a maximum baseline of 1 km. Right: Roughness (in meters) computed as the corresponding slope-detrended standard deviation. Gray pixels contain too few (< 5) MLA footprints for the analysis.

We also searched for signatures of ice in the slope and roughness characteristics of Prokofiev's floor. Here again we use the MLA footprints directly since interpolated pixels in the MLA-only DEM could lead to biases in slope and roughness. We calculated slope and roughness by stepping through a grid with increments of 375 m, and at each grid point fitting a plane to 5 MLA footprints within 500 m. Figure 10 shows maps of the slope of the plane fit and roughness (detrended standard deviation, i.e., residuals of the plane fit) binned at 2.5 km resolution. Characterizing roughness with the detrended standard deviation has the advantage of removing most of the correlation between slope and roughness that could otherwise confound interpretation of other roughness measures such as the terrain ruggedness index and the standard deviation of elevation.

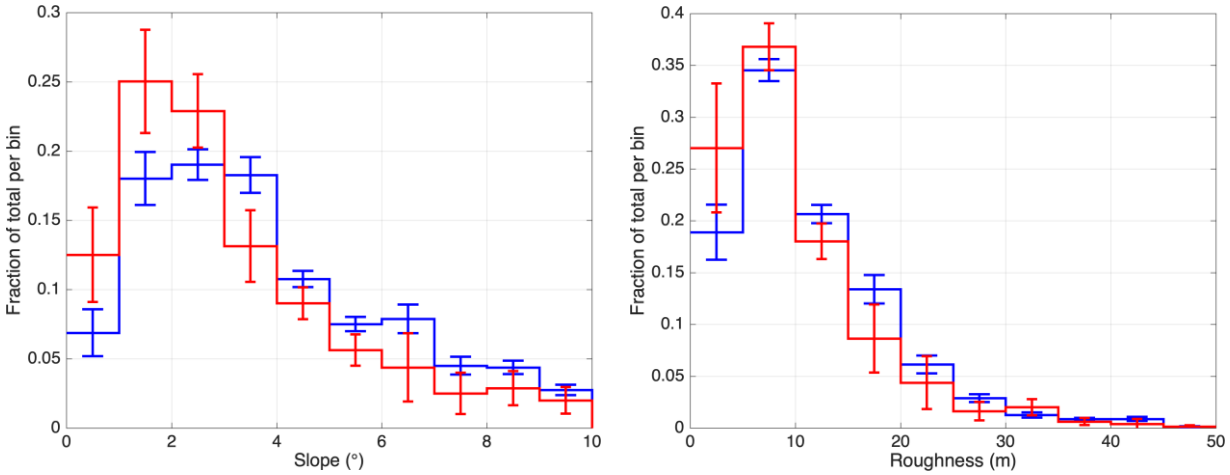

Figure 11 – Histograms of slope (left) and roughness (right) over baselines ≤ 1 km inside (red) and outside (blue) radar-bright regions within a crater-centric radius of 20 – 38 km. Error bars represent the standard deviation of a bootstrap sample size of 1000 (see text for details). Roughness is computed only for slopes < 10°.

The slope and roughness distributions inside radar-bright regions appear skewed to smaller values than outside radar-bright regions (Figure 11). The mean slope is 3.8/3.1° and the mean roughness for slopes < 10° is 11.6/10.0 m in the non-radar-bright/radar-bright regions representing differences of 0.7° and 1.6 m, respectively. To estimate the significance of these differences, we use the bootstrap sampling previously described. The observed difference in mean slope and roughness correspond to the 81st and 74th percentiles of the bootstrap sample. For comparison, the 95th percentiles of the bootstrap sample were 0.9° and 2.2 m, both larger than the observed values.

An Anderson-Darling (AD) test can also be used to assess whether the radar-bright and non-radar-bright distributions arise from the same underlying distribution. The AD test is similar to, but more powerful than, the Kolmogorov-Smirnov test (Engmann & Cousineau, 2011). If the AD test statistic is greater than the critical value for a chosen significance level, then the null hypothesis that the two distributions are drawn from the same population is rejected. Here, too, we use the bootstrap sample to estimate significance since the natural undulations in topography could lead to erroneous rejection of the null hypothesis. For the bootstrap sample, the 95th percentile AD test statistics are 32.4 and 25.4 for slope and roughness, respectively, whereas the observed values are 24.9 and 13.1, corresponding to the 82nd and 58th percentiles of the bootstrap sample.

Altogether, these tests demonstrate that, while the slope and roughness values within the radar-bright regions tend to have lower values than outside those regions, these differences do not rise to a significance threshold of 95% (p-value of 0.05) when considering the natural topographic variations throughout the entire crater floor. Table 1 lists the morphometric parameters derived in this section.

	Non-radar-bright	Radar-bright
Mean elevation (m)	-4107 ± 104	-4170 ± 67
Mean elevation residual (m)	0 ± 53	-8 ± 50
Mean slope (°)	3.8 ± 2.3	3.1 ± 2.2
Mean roughness (m)	11.6 ± 8.3	10.0 ± 7.8
Ice deposit thickness upper limit (m)	N/A	26

Table 1 – Main morphometric parameters for Prokofiev derived in this study. Errors are one standard deviation.

5 Discussion

The new illumination and thermal models presented here confirm earlier indications that the largest radar-bright region of Prokofiev extends past its PSR by up to several km. This transition region is unique on Mercury for hosting a significant radar-bright area outside permanent shadow. Our thermal models indicate that the radar-bright signal in this zone is likely due to sub-surface ice within the top ~1 – 2 m. The high crater density on Prokofiev's floor suggests that it may host small-scale, sub-resolution cold traps that allow ice to exist even closer to the surface (Rubanenko et al. 2018).

Does Prokofiev's floor contain a dark deposit like what is seen in the H20 craters? Prokofiev's T_{max} distribution (Figure 12) is shifted to lower values relative to the H20 craters and it has a significant area with T_{max} < 300 K, the approximate stability temperature of the dark deposit material hypothesized by H20 (300 ± 50 K). Therefore, we might expect Prokofiev to host a widespread dark deposit; yet visual inspection of the MDIS images does not reveal any clear signatures of one and the MLA reflectance of Prokofiev's non-radar-bright floor does not resemble that of the dark deposits (Figure 4).

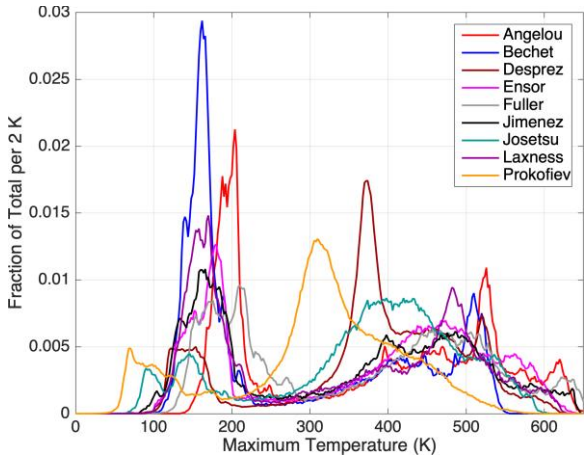

Figure 12 – Distribution of T_{max} for Prokofiev compared to that of the smaller, lower-latitude dark deposit craters studied in H20. Prokofiev's non-radar-bright floor exhibits a peak at T_{max} ~ 310 K.

Broadly speaking, each crater's T_{max} distribution in Figure 12 is bimodal with a cold peak at T_{max} < 250 K on its southern half and a hot peak at T_{max} > 250 K on its northern half. The generally higher T_{max} peak of the other craters compared to that of Prokofiev is consistent with expectations from thermal models that PSR temperatures generally increase toward lower latitudes and that small bowl-shaped craters tend to be hotter than larger, flat-floored craters (Vasavada et al. 1999). Given the lack of an obvious widespread dark deposit in Prokofiev and the fact that most of its floor has T_{max} > 250 K, the stability temperature of the dark deposit material may be closer to 250 K than 300 K. Alternatively, the lack of a dark deposit on Prokofiev's relatively warm floor compared to other craters (Figure 12) may suggest that the dark deposits are only present in areas where ice was at least temporarily stable or sub-surface ice is stable, suggesting such conditions may be needed if the dark deposit material is due to the formation of a lag deposit over stable water ice.

The MLA reflectance distribution within Prokofiev's largest PSR suggests the presence of a darker-than-ice surface material. What is this material? Two possibilities are silicates and/or organics delivered simultaneously with the ice or through subsequent impacts. If the ice is as young and as thick as hypothesized, then it seems unlikely that there has been enough time for impact gardening to bring significant quantities of silicates to the surface from below the ice (Costello et al. 2020). Chemical processing of organics by high energy radiation from Mercury's magnetosphere may also act to continuously increase the near-surface abundance of dark material (Crites et al. 2013; Delitsky et al. 2019). Ice loss through non-thermal processes, such as impact vaporization and ejection (Farrell et al. 2019) and desorption by Ly-α radiation (Morgan & Shemansky 1991) may increase the relative proportion of the dark material, as well.

According to the linear mixture models derived here, the total ice areal fraction on the surface is ~25 – 50%, suggesting that highly pure surface ice is not producing the optically-bright PSR seen in MDIS

images and MLA data. Strictly speaking, this result only applies to the MLA sensing depth, which is unknown precisely, but likely to be very small ($\lesssim$ 1 mm). Hence, the ice abundance just below the surface may be larger than this estimate. We also note again that other mixing modalities, such as intimate mixing, may hide significantly more surface ice than inferred from these linear models (Hapke 2012; Yoldi et al. 2015). However, a "dirty" surficial ice layer covering Prokofiev's largest PSR is qualitatively consistent with the dirty ice inferred from radar-scattering models (Rivera-Valentín et al. 2022) suggesting a correlation between the surface and sub-surface impurities. Previous comparisons between S-band and X-band observations of Prokofiev were reported in Harmon et al. (2011). The differences were minor for Prokofiev but suggested to possibly be due to pure surface ice not exposed directly at the surface but covered by some amount of regolith.

A major unresolved question is why the surface ice stability regions in the Moon's PSRs do not show bright reflectance features like that observed in Prokofiev (Koeber et al. 2014). In their study of the LOLA 1064 nm normal albedo in lunar south polar PSRs, Fisher et al. (2017) estimated a total ice-bearing footprint fraction of 75% and sub-footprint areal ice coverage of 7%. Assuming the same near-IR ice normal albedo (r_i = 0.8), we have found in Prokofiev an ice-bearing footprint fraction ~80 – 100% and sub-footprint areal ice coverage ~30 – 50%. This suggests that surface ice in Prokofiev is at least ~4 – 10 times more abundant than at the Moon's south pole. More generally, these results may provide an approximate minimum threshold of ice coverage for detectability by optical scattered-light imaging as done with MDIS (Chabot et al. 2014) and the Lunar Reconnaissance Orbiter Narrow Angle Camera (Koeber et al. 2014). Upcoming ShadowCam imagery from the Korean Pathfinder Lunar Orbiter spacecraft may help confirm such small areal coverages on the Moon (Robinson et al. 2018). One explanation for the presence of much more extensive ice in Mercury's polar PSRs in comparison to the Moon is that Mercury's ice is relatively young, perhaps delivered by a recent impactor, such as the one which made the rayed crater Hokusai (Ernst et al., 2018). In this scenario, as regolith gardening continues on Mercury, Mercury's volatile polar deposits may evolve to resemble those of the Moon.

Finally, we investigated three different possible topographic expressions of Prokofiev's volatile deposit, namely, average height, slope, and roughness. None of these showed a clear difference between radar-bright and non-radar-bright floor regions. Any differences that do exist are likely to be comparable to, or smaller than, the unrelated natural topographic undulations present on the crater floor. The radar-bright deposit had an overall lower elevation (-8 ± 73 m) compared to the non-radar-bright floor even after removing a long-wavelength trend. Using 5 hand-edited individual MLA tracks in Prokofiev, Susorney et al. (2019) estimated a mean elevation difference of 36 ± 60 m between radar-bright and non-radar-bright regions. We attribute the difference between their estimate and ours to the limited spatial sampling of 5 MLA tracks and the natural elevation variability on Prokofiev's floor. By combining similar measurements in 3 other radar-bright craters and comparing them to a control sample of 8 non-radar-bright craters, Susorney et al. (2019) derived an overall upper limit on the average ice deposit thickness

of 15 m. This is smaller than our upper limit of 26 m for Prokofiev, but formally it applies to the average thickness in several craters whereas the thickness in any one crater could be larger. While our limit is higher, it is more directly applicable to Prokofiev alone and it utilizes all the available MLA altimetry with reduced geolocation errors.

Regarding slope and roughness, Prokofiev's radar-bright floor tends to have lower values than its non-radar-bright floor. This is qualitatively consistent with other detections of reduced roughness in some PSRs on the Moon and Mercury (Deutsch et al. 2021a; 2021b). Those studies hypothesized this behavior may be due, on the Moon, to ice subduing surface topography and, on Mercury, to the young ages of the deposits and material property differences between ice and regolith. However, as in Prokofiev, there was considerable overlap in the roughness distributions inside and outside those PSRs due to natural topographic variations. Denser sampling of topography throughout the polar regions of both the Moon and Mercury would allow tighter constraints on the subtle surface expression of ice.

6 Conclusions

Using MDIS images and refined MLA altimetry, we derived a new high-resolution DEM of Prokofiev, which we then used to compute illumination and thermal models for this crater. The new models confirmed previous results that the largest radar-bright region in Prokofiev extends up to several kilometers past its PSR making this region unique on Mercury for hosting a significant radar-bright area outside a PSR, likely due to sub-surface ice.

The near-infrared normal albedo distribution of Prokofiev's PSR suggests the presence of a darkening agent mixed with the surface ice. Linear mixture models predict that at least roughly half of the surface area is covered with the dark material suggesting that highly pure surface ice is not producing the optically-bright deposit. The dark material may be composed of silicates or hydrocarbons contemporaneously delivered with the ice or through subsequent impacts. Chemical processing of organics by high-energy radiation and ice loss through non-thermal processes may also increase the dark material's relative abundance. This is the first estimate of the dark material's abundance specifically in Prokofiev which may be used to place limits on the age of the ice.

Using all the improved MLA altimetry available in Prokofiev, we placed an upper limit of 26 m on its ice deposit thickness. The topographic slope and roughness of the ice deposit on baselines < 1 km are lower than they are outside the deposit although the difference is not statistically significant when compared to the entire floor's topographic variations.

These results place new constraints on the nature of Prokofiev's volatile deposit that will inform future missions, such as BepiColombo. Higher-resolution topography combined with diffuse-light spectral imaging will be critical to better understand the role of small-scale cold traps and the amount of water in Prokofiev's icy upper layers.

Data Availability

The data used here can be downloaded from the NASA Planetary Data System (https://pds-geosciences.wustl.edu/), Planetary Geodesy Data Archive (https://pgda.gsfc.nasa.gov/) and the Johns Hopkins Applied Physics Laboratory Data Archive (https://lib.jhuapl.edu/papers/new-constraints-on-the-volatile-deposit-in-mercury/).

Acknowledgements

This work was funded by NASA grant 80NSSC19K0881 with additional funding from the Planetary Science Division. The material is based upon work supported by NASA under award number 80GSFC21M0002.

References

Alexandrov, O., & Beyer, R. A. 2018, E&SS, 5, 652. https://doi.org/10.1029/2018EA000390

Butler, B. J., Muhleman, D. O. & Slade, M. A. 1993, JGR, 98, 15003. https://doi.org/10.1029/93JE01581

Chabot, N. L., Ernst, C. M., Denevi, B. W., et al. 2014, Geo, 42, 1051. https://doi.org/10.1130/G35916.1

Chabot, N. L., Shread, E. E. & Harmon, J. K. 2018a, JGRE, 123, 666. https://doi.org/10.1002/2017JE005500

Chabot, N. L., Lawrence, D. J., Neumann, G. A., et al. 2018b, in Mercury: The View After MESSENGER, ed. S. C. Solomon, et al. (Cambridge, UK: Cambridge University Press), 346.

Costello, E. S., Ghent, R. R., Hirabayashi, M., Lucey, P. G., 2020, JGRE, 125, e06172. https://doi.org/10.1029/2019JE006172

Crites, S. T., Lucey, P. G. & Lawrence, D. J. 2013, Icar, 226, 1192. https://doi.org/10.1016/j.icarus.2013.08.003

Delitsky, M. L., Paige, D. A., Siegler, M. A., et al. 2017, Icar, 281, 19. https://doi.org/10.1016/j.icarus.2016.08.006

Denevi, B. W., Chabot, N. L., Murchie, S. L., et al. 2018, SSR, 214, 2. https://doi.org/10.1007/s11214-017-0440-y

Deutsch, A. N., Chabot, N. L., Mazarico, E., et al. 2016, Icar, 280, 158. https://doi.org/10.1016/j.icarus.2016.06.015

Deutsch, A. N., Neumann, G. A. & Head, J. W. 2017, GRL, 44, 9233. https://doi.org/10.1002/2017GL074723

Deutsch, A. N., Head, J. W., Chabot, N. L. & Neumann, G. A. 2018, Icar, 305, 139. https://doi.org/10.1016/j.icarus.2018.01.013

Deutsch, A. N., Heldmann, J. L., Colaprete, A., et al. 2021b, 52nd Lunar and Planetary Sci. Conf.,

2548, 2024.

Deutsch, A. N., Heldmann, J. L., Colaprete, A., et al. 2021a, PSJ, 2, 213. https://doi.org/10.3847/PSJ/ac24ff

Domingue, D. L., Denevi, B. W., Murchie, S. L. & Hash, C. D. 2016, Icar, 268, 172. https://doi.org/10.1016/j.icarus.2015.11.040

Eke, V. R., Lawrence, D. J. & Teodoro, L. F. 2017, Icar, 284, 407. https://doi.org/10.1016/j.icarus.2016.12.001

Engmann, S. & Cousineau, D. 2011, J. Appl. Quant. Methods, 6, 1.

Ernst, C. M., Chabot, N. L., & Barnouin, O. S. 2018, JGRE, 123, 2628. https://doi.org/10.1029/2018JE005552

Farrell, W. M., Hurley, D. M., Poston, M. J., et al. 2019, GRL, 46, 8680. https://doi.org/10.1029/2019GL083158

Filacchione, G., Frigeri, A., Raponi, A., et al. 2020, MNRAS, 498, 1308. https://doi.org/10.1093/mnras/staa2379

Fisher, E. A., Lucey, P. G., Lemelin, M., et al. 2017, Icar, 292, 74. https://doi.org/10.1016/j.icarus.2017.03.023

Hamill, C. D., Chabot, N. L., Mazarico, E., et al. 2020, PSJ, 1, 57 https://doi.org/10.3847/PSJ/abb1c2

Hapke, B. 2012, Theory of reflectance and emittance spectroscopy (2nd ed.; Cambridge, UK: Cambridge University Press).

Harmon, J. K. 2007, SSRv, 132, 307. https://doi.org/10.1007/s11214-007-9234-y

Harmon, J. K., Slade, M. A. & Rice, M. S. 2011, Icar, 211, 37. https://doi.org/10.1016/j.icarus.2010.08.007

Koeber, S. D., Robinson, M. S. & Speyerer, E. J. 2014, 45th Lunar and Planetary Science Conference, 1777, 2811.

Lawrence, D. J., Feldman, W. C., Goldsten, J. O., et al. 2013, Sci, 339, 292. https://doi.org/10.1126/science.1229953

Lucey, P. G. & Riner, M. A. 2011, Icar, 212, 451. https://doi.org/10.1016/j.icarus.2011.01.022

Moon, S., Paige, D. A., Siegler, M. A. & Russell, P. S. 2021, GRL, 48, e90780. https://doi.org/10.1029/2020GL090780

Neumann, G. A., Cavanaugh, J. F., Sun, X., et al. 2013, Sci, 339, 296. https://doi.org/10.1126/science.1229764

Paige, D. A., Siegler, M. A., Zhang, J., et al. 2010, Sci, 330, 479. https://doi.org/10.1126/science.1187726

Paige, D. A., Siegler, M. A., Harmon, J. K., et al. 2013, Sci, 339, 300. https://doi.org/10.1126/science.1231106

Rivera-Valentín, E. G., Meyer, H. M., Taylor, et al. 2022, PSJ, 3, 62. https://doi.org/10.3847/PSJ/ac54a0

Robinson, M. S. & ShadowCam Team 2018, Lunar Polar Volatiles, 2087, 5028.

Rosenburg, M. A., Aharonson, O., Head, J. W., et al. 2011, JGR, 116, E02001. https://doi.org/10.1029/2010JE003716

Rubanenko, L., Mazarico, E., Neumann, G. A. & Paige, D. A. 2018, JGRE, 123, 2178. https://doi.org/10.1029/2018JE005644

Rubanenko, L., Venkatraman, J. & Paige, D. A. 2019, NatGe., 12, 597. https://doi.org/10.1038/s41561-019-0405-8

Schorghofer, N. & Taylor, G. J. 2007, JGR, 112, E02010. https://doi.org/10.1029/2006JE002779

Schorghofer, N. & Williams, J-P. 2020, PSJ, 1, 54. https://doi.org/10.3847/PSJ/abb6ff

Shepard, M. K., Campbell, B. A., Bulmer, M. H., et al. 2001, JGR, 106, 32777. https://doi.org/10.1029/2000JE001429

Sun, X. & Neumann, G. A. 2015, IEEE Trans. on Geosci. & Rem. Sens., 53, 2860, https://doi.org/10.1109/TGRS.2014.2366080

Susorney, H. C. M., James, P. B., Johnson, C. L., et al. 2019, Icar, 323, 40. https://doi.org/10.1016/j.Icar.2019.01.016

Susorney, H. C. M., Barnouin, O. S., Ernst, C. M. & Byrne, P. K. 2017, JGRE, 122, 1372. https://doi.org/10.1002/2016JE005228

Vasavada, A. R., Paige, D. A., & Wood, S. E. 1999, Icar, 141, 179. https://doi.org/10.1006/icar.1999.6175

Warren, S. G. & Brandt, R. E. 2008, JGR, 113, D14220. https://doi.org/10.1029/2007JD009744

Yoldi, Z., Pommerol, A., Jost, B., et al. 2015, GRL, 42, 6205. https://doi.org/10.1002/2015GL064780

Zuber, M. T., Head, J. W., Smith, D. E., et al. 2012, Natur, 486, 378. https://doi.org/10.1038/nature11216